Dovepress
Taylor & Francis Group

ORIGINAL RESEARCH

The Radiosensitizing Effect of Tumor-Derived Microparticles Co-Loaded with Sorafenib and Gold Nanoparticles on Hepatocellular Carcinoma

Li Yu[1,2,*], Jiali Liu[1,*], Yiwen Fan[1,*], Xiao Hu[1,3], Xiaonan Zeng[1], Shan Luo[4], Ping Chen [1]

[1]Department of Oncology, the Affiliated Hospital of Southwest Medical University, Luzhou, Sichuan, 646000, People's Republic of China; [2]Department of Oncology, Jiangsu Cancer Hospital, Nanjing Medical University Affiliated Cancer Hospital, Nanjing, Jiangsu, 210009, People's Republic of China; [3]Oncology Treatment Center, People's Hospital of Yangjiang Affiliated to Guangdong Medical University, Yangjiang, Guangdong, 529500, People's Republic of China; [4]Tianfu Jincheng Laboratory, Chengdu, 610212, People's Republic of China

*These authors contributed equally to this work

Correspondence: Ping Chen, Department of Oncology, the Affiliated Hospital of Southwest Medical University, Luzhou, Sichuan, 646000, People's Republic of China, Email biochenp@126.com

Objective: Hepatocellular carcinoma (HCC) is a highly heterogeneous tumor with features such as high recurrence, easy metastasis, and poor prognosis, posing significant challenges for clinical treatment. In this study, we introduce a novel approach for treating HCC using tumor cell-derived microparticles (MPs) co-loaded with sorafenib and gold nanoparticles (AuNP) in combination with radiotherapy.

Methods: MPSF@AuNP was prepared by co-incubating AuNP with sorafenib, and was evaluated using dynamic light scattering (DLS), transmission electron microscopy (TEM), ultraviolet-visible spectrophotometry (UV-Vis), inductively coupled plasma optical emission spectrometry (ICP-OES), high-performance liquid chromatography (HPLC), and SDS-PAGE electrophoresis. Subsequently, their targeting ability toward hepatocellular carcinoma cells and their combined antitumor therapeutic effects with radiotherapy were investigated through in vitro and in vivo experiments, while their in vivo safety was also assessed.

Results: Our results demonstrate that co-loaded microparticles (MPSF@AuNP) can effectively deliver therapeutic agents to tumor cells through homologous targeting, improving the bioavailability of therapeutic drugs and enhancing their cytotoxicity against tumor cells. Furthermore, the combination of MPSF@AuNP with radiotherapy shows a synergistic anti-tumor effect by enhancing the inhibition of tumor cell proliferation, promoting tumor cell apoptosis, remodeling the tumor microenvironment, and activating the anti-tumor immune responses.

Conclusion: This study offers a promising treatment approach for malignant tumors such as HCC by using MP co-loaded and delivered with anti-tumor drugs and AuNP in combination with radiotherapy.

Keywords: hepatocellular carcinoma, HCC, tumor-derived microparticles, MPs, sorafenib, gold nanoparticles, AuNP

Introduction

Liver cancer is one of the prevalent malignant tumors, and its incidence has risen globally in recent years. In 2022, liver cancer ranked as the third leading cause of cancer-related deaths worldwide and the sixth most frequently diagnosed cancer, with approximately 865,000 new cases and 757,948 deaths reported.[1] Currently, the treatment modalities for liver cancer include surgical resection, ablation therapy, transarterial chemoembolization (TACE), radiation therapy, molecularly-targeted drug therapy, immunotherapy and chemotherapy.[2–8] Within this therapeutic spectrum, systemic anti-tumor therapy remains the maintains its position as the cornerstone for advanced liver cancer. Specifically, most liver cancer patients are already in the locally advanced or metastatic progression at the time of diagnosis, unable to undergo effective treatment using traditional surgical methods or TACE, with limited effects from chemotherapy.[1,2,9] The emergence of molecularly targeted drugs has ushered in a transformative phase for advanced liver cancer patients. Targeted therapy drugs such as sorafenib, lenvatinib and donafenib have significantly improved treatment outcomes for patients.[10–13]

Among them, sorafenib became the first small-molecule targeted drug for clinical use in liver cancer in 2007.[13–15] Sorafenib is a multi-target receptor tyrosine kinase inhibitor that inhibits cell division and proliferation by blocking the RAF/MEK/ERK signaling pathway. It also suppresses tumor angiogenesis by targeting VEGFR-2/PDGFR-β, thereby inhibiting tumor growth.[14] Sorafenib has been approved by the FDA (Food and Drug Administration) for first-line treatment of liver cancer and can significantly improve the quality of life for patients with advanced liver cancer.[3,16] However, the side effects and acquired resistance of sorafenib hinder its clinical application.[17–19] Strategic optimization through tumor-targeted delivery systems may concurrently improve therapeutic safety and antitumor efficacy.

Extracellular vesicles (EVs) are nanoscale vesicles secreted by living cells, serving as natural carriers for transporting lipids, proteins, nucleic acids, and other biomolecules to facilitate intercellular communication.[20–23] These vesicles can be divided into three main subtypes based on their size: exosomes (30–150 nm), microparticles (100–1000 nm), and apoptotic bodies (100 nm – 5 μm).[24] Particularly noteworthy, microparticles show promise as natural carriers for drugs due to their suitable size, abundance, accessibility, and delivery efficiency.[25,26] Recent studies have shown that microparticles derived from tumor cells (TMPs) possess advantages such as superior biocompatibility, structural integrity, and tumor-homing specificity as natural drug carriers for cancer treatment, demonstrating great potential for clinical applications.[27] In addition, TMPs naturally harbor tumor-associated antigens and DNA, which can effectively promote the maturation of dendritic cells, thereby eliciting anti-tumor immune responses and achieving synergistic anti-tumor treatment effects.[28–30]

Radiation therapy (RT) is one of the commonly used methods for cancer treatment, mainly by damaging the DNA of tumor cells, promoting tumor cell death, and thus exerting anti-tumor therapeutic effects.[31,32] Recent research demonstrates that radiation therapy also contributes to the release of tumor-associated antigens, thereby boosting the effectiveness of anti-tumor immune therapy.[33–37] Notwithstanding these benefits, the use of high-dose X-rays in radiotherapy can damage surrounding healthy tissues due to high-energy ionizing radiation, constraining its clinical application.[32,38] Consequently, a key challenge in this field is to develop effective methods for increasing the radiation dose specifically in tumor tissues while minimizing damage to normal tissues caused by radiation therapy.[39] Current investigations shows that some inorganic materials can increase the energy deposition of radiotherapy doses in tumor tissues, acting as radiosensitizers.[40] Among these materials, gold nanoparticles have a higher atomic number, which enables them to absorb, scatter, and emit radiation energy, enhancing the accumulation of radiation doses in tumors and enabling their use as radiosensitizers.[41–49] Nevertheless, chemically synthesized AuNP often carry inherent biosafety concerns due to residual toxic precursors from imperfect synthesis purification Gold nanoparticles derived from cellular reduction reactions that convert gold ions to gold atoms have been used as a novel radiation sensitizer due to their high biocompatibility and good homologous targeting.[50,51]

In this study, we used tumor cell-derived microparticles to encapsulate sorafenib (MP-SF), and through co-incubation protocol with gold nanoparticles (AuNP), sorafenib was wrapped together with the gold nanoparticles in the micro-particles, preparing a dual-loaded nano-drug (MPSF@AuNP), which was then used in combination with radiotherapy for the treatment of HCC (Scheme 1). Due to the high biocompatibility of the TMPs and tumor cells, it can enhance the targeting of MPSF@AuNP to tumor cells, promoting the accumulation of the loaded drugs at the tumor site. Furthermore, AuNP function as radiosensitizers by enhancing localized radiation energy deposition in tumor tissues. Collectively, this synergistic therapeutic strategy demonstrates enhanced antitumor efficacy and represents a promising paradigm for innovative HCC treatment approaches.

Materials and Methods
Reagents and Materials
Sorafenib (Cat# S7397) was purchased from Selleck Chem. Chloroauric acid solution (HAuCl4) was purchased from Aladdin (China). Dulbecco's Modified Eagle's medium (DMEM) was acquired from Shanghai Yuanpei Biotechnology Co. (China). Fetal bovine serum was bought from GIBCO (USA). Methylthiazolium tetrazolium (MTT) was from Guangzhou Saiguo Biotechnology Co. (China). Annexin V-FITC/propidium iodide (PI) kit (Cat# 556547) used for flow cytometry analysis was from BD Bioscience (USA). Acetonitrile (HPLC grade) were purchased from Chengdu Kolon Chemical Co. (China). CD4 antibody (Cat# 25229) and CD8 antibody (Cat# 98941) were from CST (USA). CD86 antibody (Cat# LS-C392134) was from LSBio (USA). CD206 antibody (Cat# AF2535) was from BD Pharmingen
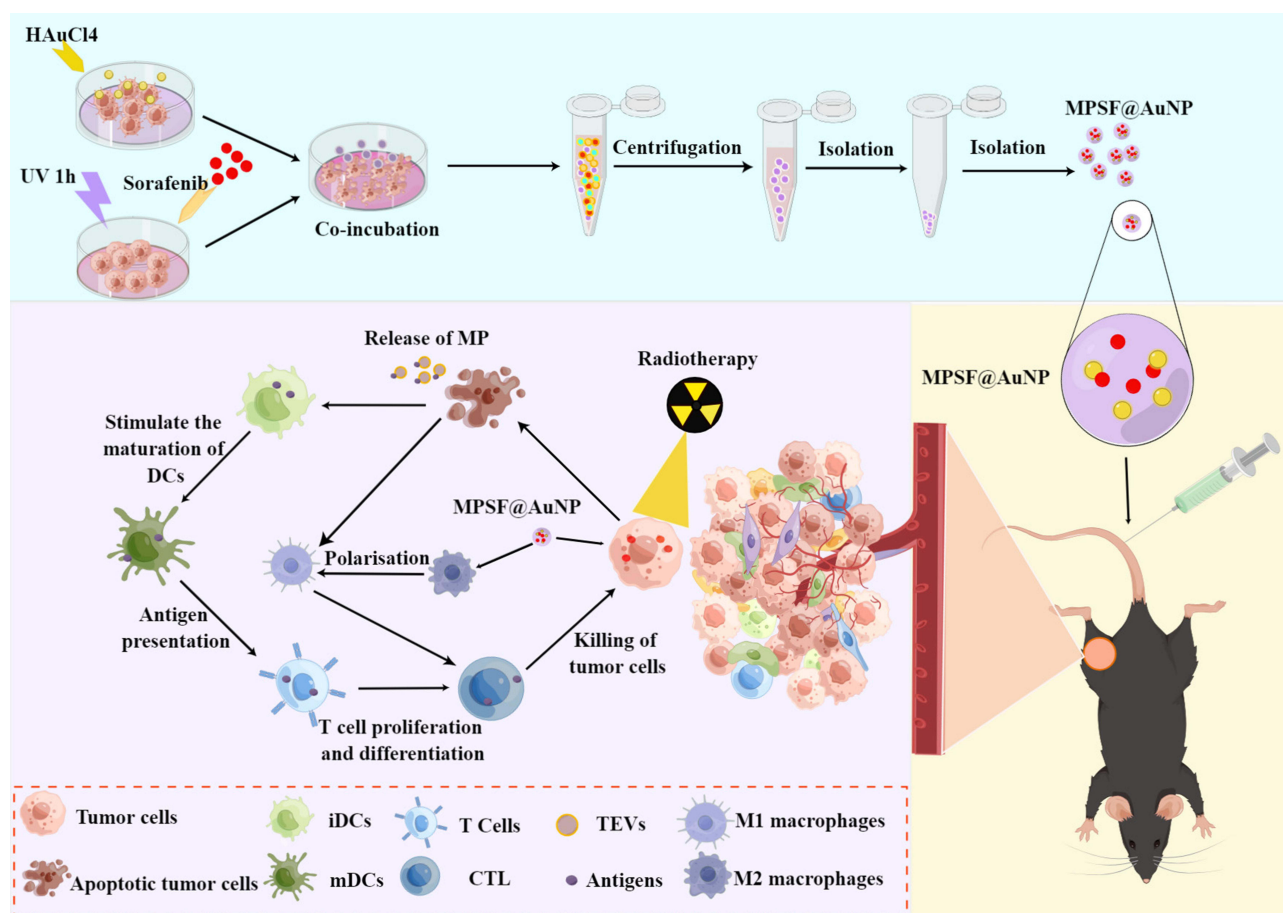
Scheme 1 Schematic diagram of antitumor mechanism of MPSF@AuNP combined with radiotherapy. This image was created using Figdraw (https://www.figdraw.com/).

(USA). Hepa 1–6 cells and Hep G2 cells were provided by American Type Culture Collection (ATCC, USA) and stored at the Experimental Medicine Center of the Affiliated Hospital of Southwest Medical University (China). Male C57BL/6J mice (18–20 g, 6–8 weeks old) were purchased from Chongqing Tengxin Biotechnology Co. (China). All animals were handled in strict accordance with the ethical standards set by relevant animal welfare agencies. The in vivo experiments adhered to the guidelines of the Animal Ethics Committee, and the animal experimental protocols were approved by the Animal Care and Treatment Committee of Southwest Medical University (China).

Preparation and Characterization of AuNP

The intracellular synthesis of gold nanoparticles was conducted according to previously published literature with minor modifications.[51] Briefly, Hep G2 or Hepa 1–6 cells were seeded in 10 cm tissue culture dishes. When the cell density reached 80%, the cells were washed twice with PBS to remove residual complete medium. Subsequently, 5 mL of 1 mM $HAuCl_4$ was added, and the cells were then incubated at 37 °C in a 5% CO_2 incubator for 3 days. The supernatant was centrifuged at 600g for 10 min to remove cell debris and aggregates. The supernatant was then centrifuged at 13,000g for 1 hour to obtain the tumor cell-derived AuNP. The morphology of AuNP was observed by transmission electron microscopy (TEM, JEM1200EX, JEOL, Japan). The UV absorption spectrum of AuNP was detected by UV spectrophotometry (UV-5800PC, Shanghai Metash Instruments Co., Ltd., Shanghai, China). Particle size and zeta potential were determined using dynamic light scattering (DLS, NanoBrook90 plus Zeta, Brookhaven, NY). The in vitro stability of AuNP in DMEM was monitored by measuring particle size. Quantitation of Au in AuNP were determined by inductively coupled plasma mass spectrometry[51] (ICP-MS, ICPOES730, Agilent, USA).

Preparation and Characterization of MP-SF

The preparation method for MP-SF is as follows:[27] collect cells in exponential growth phase, suspended the cells in serum-free DMEM, and adjust the final density to 1×10^7 cells/mL. Exposed the cell suspension to ultraviolet light (UBV, 300 J/m^2) for 1 h, then added sorafenib to a final concentration of 500 μM, and incubated in a 37 °C, 5% CO$_2$ incubator for 16 h. Subsequently, use the multiple-step centrifugation to collect the precipitate of MP-SF, first centrifuging at 600g for 10 min to remove tumor cells, then at 14,000g for 2 min to remove cell debris, and finally at 14,000g for 1 h to obtain MP-SF.[25,27,52–55]

The morphology of MP-SF and MPs were observed by TEM (JEM1200EX, JEOL, Japan). Particle size and zeta potential were determined using DLS (NanoBrook90 plus Zeta, Brookhaven, NY). The in vitro stability of MP-SF in DMEM was monitored by measuring particle size. Quantitation of sorafenib in MP-SF was determined by High Performance Liquid Chromatography[56,57] (HPLC, Agilent 1260, Agilent Technologies, USA).

Preparation and Characterization of MPSF@AuNP

Tumor cells were collected and suspended in serum-free DMEM at a density of 1×10^7 cells/mL. Irradiated the cells with ultraviolet irradiation (UBV, 300 Jm^{-2}) for 1 h, then AuNP (16 μg/mL) and sorafenib (16 μM) were added and co-incubated in a 37 °C, 5% CO$_2$ incubator for 16 h. Subsequently, following the aforementioned method, centrifuge to collect MPSF@AuNP, first centrifuging at 600g for 10 min to remove tumor cells, then at 14,000g for 2 min to remove cell debris, and finally at 14,000g for 1 h to obtain MPSF@AuNP.

The morphology of MPSF@AuNP was observed by TEM (JEM1200EX, JEOL, Japan). Particle size and zeta potential were determined using DLS (NanoBrook90 plus Zeta, Brookhaven, NY). The in vitro stability of MPSF@AuNP in DMEM was monitored by measuring particle size. Quantitation of sorafenib in MPSF@AuNP were determined by High Performance Liquid Chromatography (HPLC, Agilent 1260, Agilent Technologies, USA). Quantitation of AuNP in MPSF@AuNP were determined by inductively coupled plasma emission spectroscopy (ICPOMS, Agilent ICPOES730, USA). Using SDS-PAGE gel electrophoresis to analyzed the protein composition of MPs, AuNP, MP-SF and MPSF@AuNP, and compared them with the parental cells.

In Vitro Cellular Uptake

To investigate the efficiency of cellular uptake of the delivered drugs, we treated cells with MPs derived from tumor cells loaded with the fluorescent dye coumarin 6.[58] The cells were seeded in 6-well plates at a density of 5×10^5 cells per well and cultured overnight. Prepared MP-coumarin 6 (100 μg/mL) or free coumarin 6 (100 μg/mL) were co-cultured with the cells for 4 hours. After removing the supernatant, the cells were fixed with 4% paraformaldehyde for 15 min, followed by DAPI staining for 5–10 min. The uptake of coumarin 6 by tumor cells was observed using a fluorescence microscope (OLYMPUS, IX73, Japan). The fluorescence intensity of internalised coumarin 6 was quantified using flow cytometry (BD FACSVerse, Piscataway, NJ).

In Vitro Cytotoxicity Assays

Tumor cells (5×10^5 cells/well) were seeded in 6-well plates and cultured overnight. Subsequently, the cells were treated with DMEM, MPs (tumor-cell-derived microparticles), AuNP (Au-loaded tumor-cell-derived extracellular vesicles, final Au concentration 16 μg/mL), SF (sorafenib, 16 μM), MP-SF (sorafenib-loaded tumor-cell-derived microparticles, final sorafenib concentration 16 μM), RT (radiotherapy, 6 Gy), RT-AuNP (radiotherapy, 6 Gy; Au loaded tumor-cell-derived extracellular vesicles, final Au concentration 16 μg/mL), and RT-MPSF@AuNP (radiotherapy, 6 Gy; sorafenib- and Au- loaded tumor-cell-derived microparticles, final sorafenib concentration 16 μM, final Au concentration 16 μg/mL), respectively. The cell status was observed and photographed using a microscope at 0 h, 24 h, 48 h and 72 h after the initiation of treatment.

Regarding MTT assay, Hepa 1–6 or Hep G2 cells (5×10^5 cells/well) were seeded in 6-well plates and cultured overnight. Subsequently, they were treated with DMEM, MPs, AuNP, SF, MP-SF, RT, and RT-AuNP, and RT-MPSF@AuNP, respectively. After 72 h of treatment, 10 μL of MTT solution (5 mg/mL) was added to each well. The plate was then incubated at 37 °C in the dark for 4 hours, and the supernatant was discarded. Next, 150 μL of dimethyl sulfoxide (DMSO) was added to each well to dissolve the crystals. The OD values were quantitatively measured at 490 nm using a microplate reader (iMark Bio-Rad, CA, USA).

In Vitro Wound Healing

In vitro wound healing was used to study the impact of different treatments on the invasive ability of tumor cells. Cells were seeded in 6-well plates at a density of 5×10^5 cells per well. After the cells adhere to the plate, the midline of the culture wells was longitudinally scratched using a sterile pipette tip. Fresh culture medium was added after washing off the detached cells. The cells were treated with DMEM, MPs, AuNP, SF, MP-SF, RT, and RT-AuNP, and RT-MPSF@AuNP, respectively. The wound coverage was observed under a microscope and photographed. The scratch healing rates of the treatment groups at 24 h, 48 h and 72 h post-scratching were calculated.

In Vitro Apoptosis Assays

The cells were seeded in six-well plates at a density of 5×10^5 cells/well and incubated in a 37 °C, 5% CO_2 incubator for 24 h. Subsequently, the cells were treated with DMEM, MPs, AuNP, SF, MP-SF, RT, and RT-AuNP, and RT-MPSF@AuNP for 72 h. Following the manufacturer's instructions, flow cytometry analysis was performed using an Annexin V FITC/propidium iodide (PI) assay kit. Briefly, the cells were harvested, suspended in 200 μL binding buffer, and incubated with 5 μL Annexin V FITC and 5 μL propidium iodide for 15 min. The percentage of live and apoptotic cells was assessed using flow cytometry (BD FACSVerse, Piscataway, NJ).

In Vivo Fluorescence Imaging

Gold nanoparticles (AuNP) were initially prepared according to the aforementioned protocol. Indocyanine green (ICG) was substituted for SF during the synthesis. Tumor cells, pre-irradiated with ultraviolet light for 1 hour, were incubated with ICG and AuNP in a constant-temperature incubator for 16 hours. MP-ICG@AuNP complexes were subsequently isolated via differential centrifugation. When tumor volumes reached 100 mm³, mice were intravenously administered free ICG or MP-ICG@AuNP (ICG dose: 1 mg/kg). NIR-II fluorescence imaging was performed 12 hours post-injection using a dedicated imaging system.

In Vivo Immune Stimulation Assay

Hepa1-6 cells (5×10^6 cells per mouse) were subcutaneously inoculated into the right leg of C57 mice to establish hepatocellular carcinoma (HCC) xenograft models. Upon tumor volumes reaching 100 mm³, mice were randomized into eight treatment groups. One week post-treatment, tumor tissues were harvested, digested, and centrifuged to isolate tumor-infiltrating cells. The cell suspension (500 μL per tube) was incubated with anti-CD3 (1 μL), anti-CD8a (1 μL), and anti-CD4 (1 μL) antibodies for 20 min. $CD3^+CD4^+$ and $CD3^+CD8^+$ T-cell populations were quantified via flow cytometry.

In vivo Anti-Tumor Efficacy of MPSF@AuNP Combined with Radiotherapy

To evaluate the antitumor effect of MPSF@AuNP combined with radiotherapy in HCC, 5×10^6 Hepa 1–6 cells were subcutaneously injected into the right leg of C57BL/6J mice. Once the mean tumor volume reached 100 mm³, the mice were randomly divided into eight groups (n = 10 per group): (1) PBS (phosphate-buffer saline); (2) MPs (tumor-cell-derived microparticles); (3)AuNP (Au-loaded tumor cell-derived extracellular vesicles, 1mg/kg); (4) SF (sorafenib, 5 mg/kg); (5) MP-SF (sorafenib-loaded tumor cell-derived microparticles, 5 mg/kg sorafenib); (6) RT (radiotherapy, 6 Gy); (7) RT-AuNP (radiotherapy, 6 Gy; Au-loaded tumor cell-derived extracellular vesicles, 1 mg/kg); (8) RT-MPSF@AuNP (radiotherapy, 6 Gy; sorafenib-loaded tumor cell-derived microparticles, sorafenib 5 mg/kg; Au-loaded tumor cell-derived extracellular vesicles, Au 1 mg/kg). The SF group received sorafenib via gavage every four days for a total of three doses. Mice in the PBS, MPs, AuNP, MP-SF, and MPSF@AuNP treatment groups were administered the corresponding drugs via tail vein injection every four days, for a total of three injections. Radiotherapy was performed 24 hours after each injection, amounting to three sessions total. Tumor size was measured every other day using calipers, and tumor volumes were calculated according to the formula: V = 1/2 × length × width × width. Six mice per group were used to assess survival. For histological analysis, mice were euthanized on day 4 after completion of treatment. Tissues of heart, liver, spleen, lungs, kidneys and excised tumors were collected from each treatment group and fixed in 10% neutral buffered formalin.

^{18}F-FDG Micro-PET/CT Imaging

To assess the early tumor treatment efficacy of the RT-MPSF@AuNP, ^{18}F-FDG micro-PET/CT scanning (Siemens, Germany) was performed 24 h after completion of treatment, following a fasting period of over 6 hours for the mice. Subsequently, the mice were anesthetized for 30 min using isoflurane. They were placed on the scanning bed, secured with tape, and positioned at the center of the scanning field. Scanning was conducted using the following parameters: current of 500 mA, voltage 80 kV, a duration of 10 minutes per bed position, and a layer thickness of 1.5 mm. Regions of interest (ROIs) in the PET/CT images were delineated by two experienced specialists. The hottest pixel within the tumor was used to calculate the maximum standardized uptake value (SUVmax) and the mean uptake value (SUVmean) for the tumor region.

Assessment of in Vivo Safety

By conducting blood biochemical and blood routine tests on the whole blood of mice, the effects of the treatment on liver and kidney function, as well as on the hematological system, were investigated. Blood from the eye was collected in a coagulation tube, allowed to sit for about 1 h, and then centrifuged at 3,000g for 10 min to collect upper plasma layer. The analysis included ALT (alanine aminotransferase), AST (aspartate aminotransferase), ALB (albumin), urea and Crea (creatinine) to assess the liver and kidney function of mice. Blood was also collected from the eye using an anticoagulant tube, and specialized equipment used to perform WBC (white blood cells), RBC (red blood cells), and PLT (platelets) tests to evaluate the impact of the treatment on the hematological system.

Histology and Immunohistochemistry Assays

Tumors and organs (heart, liver, spleen, lung and kidney) were collected from each group of mice, fixed in 4% paraformaldehyde, and embedded in paraffin. Histopathological assessments were conducted using hematoxylin-eosin (H&E) staining to evaluate lesions in various organs after drug treatment. The ELF 97 Immunohistochemistry Kit (ThermoFisher, E6600) was used for immunohistochemical staining. The primary antibodies used in this study included anti-CD4 (1:200), anti-CD8 (1:200), anti-CD86 (1:200), and anti-CD206 (1:200).

Statistical Analysis

Statistical analysis was conducted using GraphPad Prism 9 (GraphPad Software, Inc). Comparisons between two groups were made using the Student's *t*-test, while one-way analysis of variance (ANOVA) was employed for multiple group comparisons. Survival curves were generated using the Kaplan–Meier method, with statistical significance evaluated through the Log rank test. Results were presented as mean ± SEM, and *P*-values <0.05 were considered statistically significant.

Results

Manufacturing and Characterization of AuNP, MPs, MP-SF and MPSF@AuNP

AuNP, MP-SF and MPSF@AuNP were prepared using the described methods. As shown in Figure 1A–E, the optimal concentration of HAuCl4 for producing AuNP was determined to be 1 mM, with an ideal incubation time of 72 h. As incubation time increased, the color of the supernatant darkened to a purplish-black, and an absorption peak was observed at 540 nm (Figure S1A and B). Additionally, microscopic observation revealed that the cells maintained their morphology and exhibited a purple-red color (Figure S1C and D). We employed high-performance liquid chromatography (HPLC) to analyze the sorafenib loading in MP-SF and MPSF@AuNP (Figure S2A–D). Based on an assessment of both the drug loading capacity and the cytotoxicity of sorafenib, we selected a concentration of 500 μM for preparing MP-SF and MPSF@AuNP in this study.

The morphology of the nanoparticles was characterized by TEM, while DLS was used to measure particle size and zeta potential. TEM images indicated that AuNP displayed a homogeneous black spherical shape, MPs and MP-SF had a consistent mono-globular morphology, and MPSF@AuNP exhibited an irregular globular form (Figure 1F–H). DLS measurements revealed that the particle sizes of AuNP, MPs, MP-SF, and MPSF@AuNP were 60.87 ± 2.03 nm, 199.73 ± 0.85 nm, 217.43 ± 1.55 nm and 301.83 ± 4.75 nm (Figure 1I and J), respectively. Correspondingly, the zeta potentials were found to be 0.64 ± 0.02 mV for AuNP, −3.55 ± 0.05 mV for MPs, −2.78 ± 0.09 mV for MP-SF, and 1.66 ± 0.15 mV for
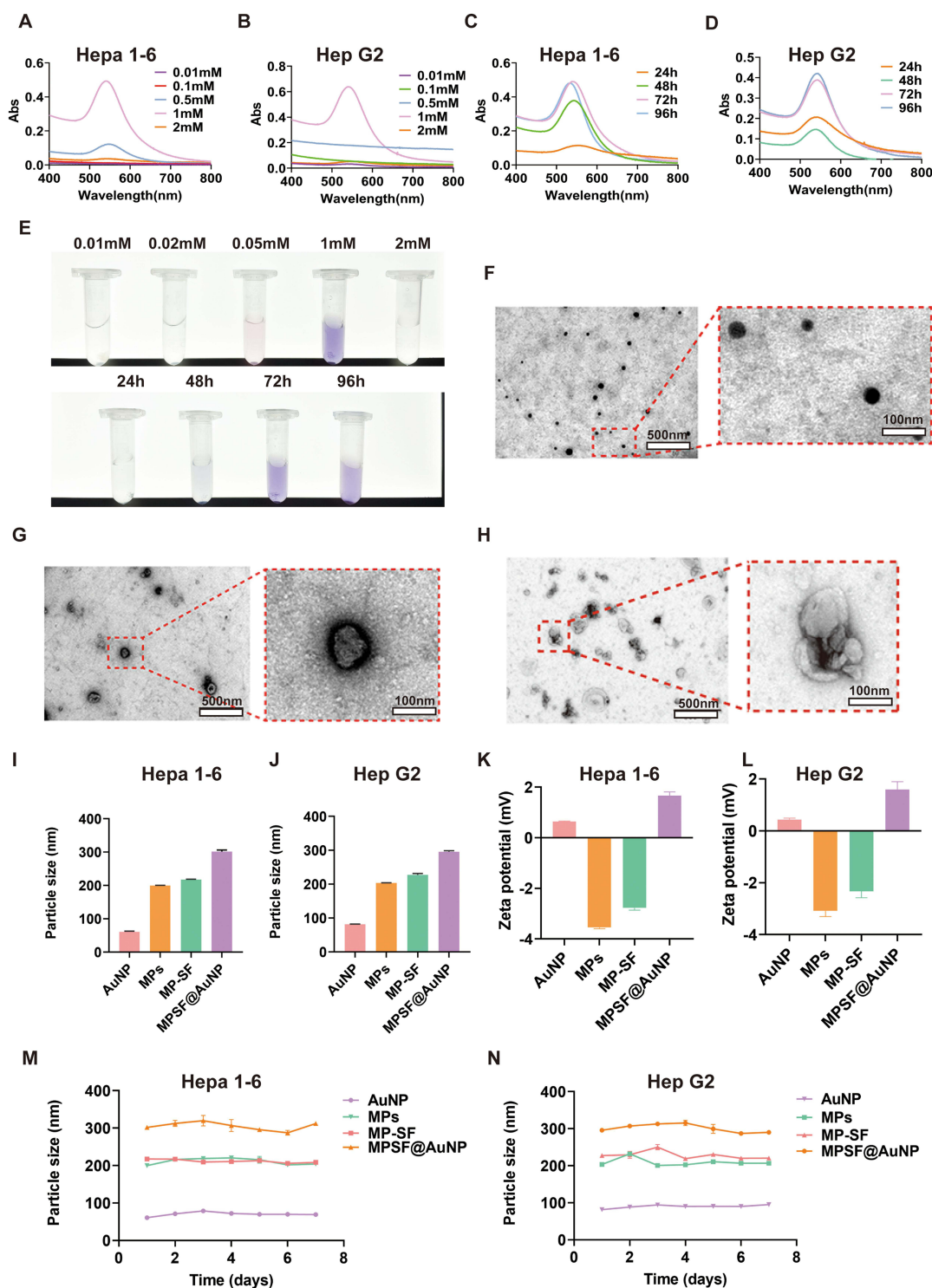
Figure 1 Manufacture and characterisation of MPSF@AuNP. (**A**) The ultraviolet spectrum after incubating Hepa 1–6 cells with different concentrations of HClAu4. (**B**) The ultraviolet spectrum after incubating Hep G2 cells with different concentrations of HClAu4. (**C**) The ultraviolet spectrum after incubating Hepa 1–6 cells with 1 mM HClAu4 for different durations. (**D**) The ultraviolet spectrum after incubating Hep G2 cells with 1 mM HClAu4 for different durations. (**E**) The upper image shows the color changes after incubating Hepa 1–6 cells with different concentrations of HClAu4, while the lower image shows the color changes after incubating Hepa 1–6 cells with 1 mM HAuCl4 for different durations. (**F**) Transmission electron micrographs of AuNP. Scale bars, 500 nm and 100 nm, respectively. (**G**) Transmission electron micrographs of MP (nonloaded microparticles). Scale bars, 500 nm and 50 nm, respectively. (**H**) Transmission electron micrographs of dual-carrier MPSF@AuNP. Scale bars, 500 nm and 100 nm, respectively. (**I**) Particle sizes of AuNP, MPs, MP-SF, and MPSF@AuNP (derived from Hepa 1–6 cells) (n=3). (**J**) Particle sizes of AuNP, MPs, MP-SF, and MPSF@AuNP (derived from Hep G2 cells) (n=3). (**K**) Zeta potentials of AuNP, MPs, MP-SF, and MPSF@AuNP (derived from Hepa 1–6 cells) (n=3). (**L**) Zeta potentials of AuNP, MPs, MP-SF, and MPSF@AuNP (derived from Hep G2 cells) (n=3). (**M**) The stability of particle size of MPs, MP-SF, AuNP, and MPSF@AuNP in DMEM was tested for 7 days at 25°C (derived from Hepa 1–6 cells) (n=3). (**N**) The stability of particle size of MPs, MP-SF, AuNP, and MPSF@AuNP in DMEM was tested for 7 days at 25°C (derived from Hep G2 cells) (n=3). Data are presented as the mean ± SEM.

MPSF@AuNP (Figure 1K and L). Compared to MP-SF, MPSF@AuNP encapsulated AuNP, resulting in a slightly larger particle size. The positive zeta potential of MPSF@AuNP may be attributed to the presence of AuNP within the structure.

To investigate the stability of AuNP, MPs, MP-SF and MPSF@AuNP, measured the particle size changes of these samples in DMEM over a period of 7 days using DLS. The results showed no significant variations in particle size for AuNP, MPs, MP-SF, and MPSF@AuNP during the testing period (Figure 1M and N), suggesting that the nanoparticles exhibited good stability. SDS-PAGE analysis of protein fractions derived from the nanoparticles revealed that MPs, AuNP, MP-SF, and MPSF@AuNP displayed similar protein profiles. Furthermore, corresponding protein profiles were detected in the parental tumor cells, indicating that the microparticles retained various tumor-associated antigens from the original tumor cells (Figure S3A and B).

In vitro Uptake Efficiency and Cytotoxicity Analysis

To investigate the efficiency of cellular uptake of free versus MP-loaded drugs in vitro, we utilized coumarin 6 (C6)-labeled MPs (MP-C6) and compared the cellular uptake of free C6 with MP-C6 using fluorescence microscopy and flow cytometry. As shown in Figure 2A–D, cells treated with MP-C6 exhibited significantly higher levels of green fluorescence compared to those treated with free C6. Flow cytometry results corroborated the findings from fluorescence microscopy (Figure 2B–E). Quantitative analysis revealed that the fluorescence intensities for control, C6-treated and MP-C6-treated Hepa 1–6 and Hep G2 cells were 12425.50 ± 4306.72 / 3542.63 ± 111.48, 572,049.90 ± 13,344.32 / 44,507.63 ± 477.49 and 2852329.67 ± 35,484.25 / 184,155.53±1900.58, respectively (Figure 2C–F). These results indicate that MPs have high biocompatibility with tumor cells and can effectively enhance the uptake of drugs by tumor cells.

To determine whether MPSF@AuNP could enhance the cytotoxicity of radiotherapy (RT) on tumor cells, we introduced MPSF@AuNP derived from the corresponding cells into Hepa 1–6 or Hep G2 cells prior to radiotherapy. After 24, 48, and 72 h of treatment, we examined the status of the tumor cells microscopically. Compared to the control group, treatments with SF, MP-SF, RT, RT-AuNP, and RT-MPSF@AuNP all inhibited tumor cell growth and increased cell mortality, with the RT-MPSF@AuNP group showing the strongest effect (Figures S4 and S5). Further MTT assay revealed that SF, MP-SF, RT, RT-AuNP, and RT-MPSF@AuNP effectively suppressed tumor cell proliferation (Figure 2G and H). Notably, MP-SF exhibited greater cytotoxicity at the same dose compared to free SF, suggesting that encapsulating the drug in MPs enhances its tumor-killing efficiency. Additionally, the cytotoxicity of MPSF@AuNP combined with radiotherapy was significantly greater than that of MPSF@AuNP or RT alone, indicating a synergistic effect between MPSF@AuNP and radiotherapy in inhibiting cell proliferation. In conclusion, these findings align with our previous studies, demonstrating that tumor cell-derived microparticles can effectively encapsulate antitumor agents, enhance drug absorption by tumor cells, and more effectively inhibit tumor cell proliferation. Moreover, the combination of MPSF@AuNP with radiotherapy further amplifies the inhibitory effects on tumor cell growth.

Cell Migration Assays

In vitro wound healing assays were performed to assess the inhibition of tumor cell migration in different treatment group. As shown in Figure 3A–D, the wound areas in the control, MPs, and AuNP treatment groups exhibited significant recovery after 72 h. However, free SF showed a certain inhibitory effect on cell migration, while the MP-SF group exhibited a more pronounced effect, with migration rates of 43.73% for Hepa 1–6 cells and 30.85% for Hep G2 cells at 72 hours. Additionally, the cell migration rate in the RT-AuNP group was lower than that in the radiotherapy-only group, with migration rates of 43.14% for Hepa 1–6 cells and 31.37% for Hep G2 cells at 72 hours. In contrast, the RT-MPSF@AuNP group nearly completely inhibited cell migration, recording the lowest migration rates of 23.41% for Hepa 1–6 cells and 10.42% for Hep G2 cells at 72 h. These findings indicate that the combined radiotherapy strategy employing MPSF@AuNP has the most significant inhibitory effect on tumor cell migration.

Induction of Apoptosis in vitro

Flow cytometry analysis indicated that, compared to the control group (10.93 ± 1.47% and 23.59 ± 4.09%, respectively), there was no significant change in the apoptosis rates of Hepa 1–6 and Hep G2 cells after treatment with MPs (11.86 ± 0.32% and 27.13 ± 3.95%, respectively) or AuNP (12.21 ± 1.20% and 27.01 ± 3.63%, respectively), suggesting that MPs or AuNPs did not exhibit significant toxicity to the cells (Figure 4A–D). The apoptosis rates in the MP-SF treatment group (47.83 ± 1.84%

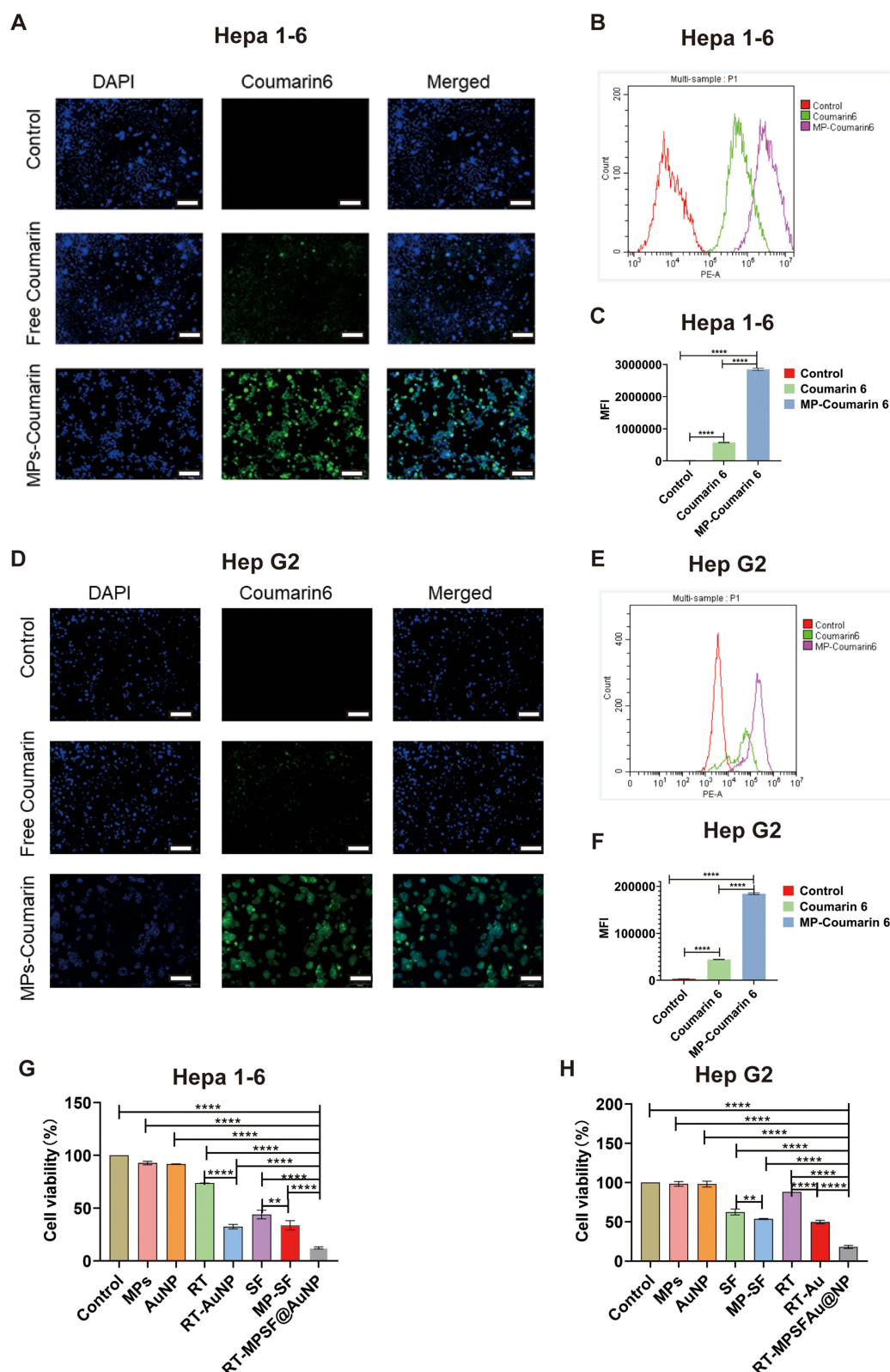**Figure 2** In vitro cellular uptake and cytotoxicity analysis. (**A**) Fluorescence microscopy images of Hepa1-6 cells ingesting free coumarin 6 and MP-coumarin 6. Scale bar, 200 μm. (**B**) Flow cytometry analysis of free coumarin 6 and MP-coumarin 6 uptake by Hepa1-6 cells. (**C**) Flow cytometry analysis corresponding relative mean fluorescence intensity (MFI), and the results are the mean ± SEM of three replicates (Hepa 1–6 cell source). (**D**) Fluorescence microscopy images of Hep G2 cells ingesting free coumarin 6 and MP-coumarin 6. Scale bar, 200 μm. (**E**) Flow cytometry analysis of free coumarin 6 and MP-coumarin 6 uptake by Hep G2 cells. (**F**) Flow cytometry analysis corresponding to the relative mean fluorescence intensity (MFI), and the results are the mean ± SEM of three replicates (Hep G2 cell source). (**G**) The cell viability of Hepa 1–6 cells in various treated groups was analyzed using the MTT method, the results are the mean of three replicates ± SEM. (**H**) The cell viability of Hep G2 cells in various treated groups was analyzed using the MTT method, the results are the mean of three replicates ± SEM. ** represents $P < 0.01$, and **** represents $P < 0.0001$.
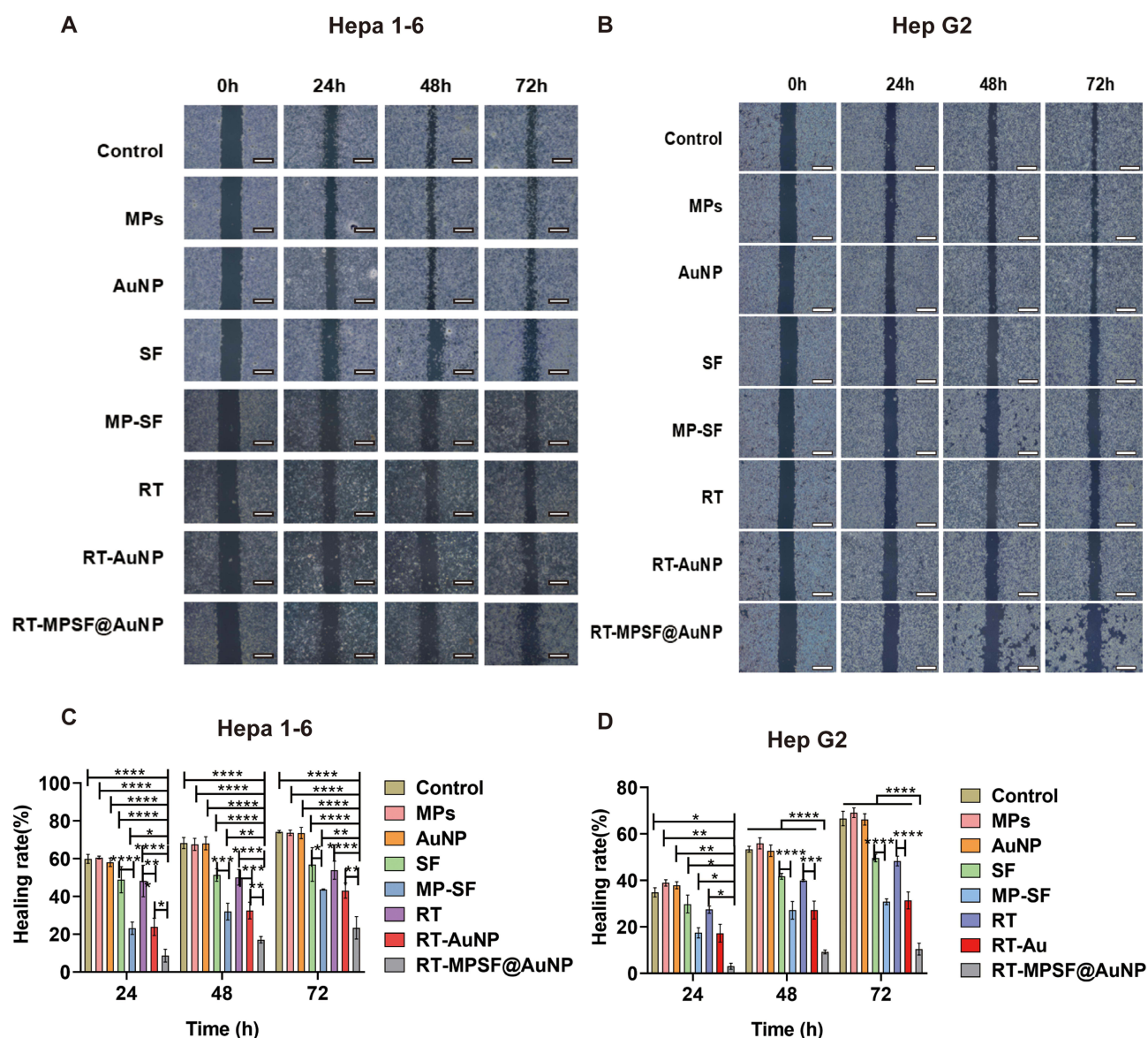
Figure 3 Cell migration assays. (**A**) Wound healing images of Hepa 1–6 cells. Scale bar, 200 μm. (**B**) Wound healing images of Hep G2 cells. Scale bar, 200 μm. (**C**) Healing rates were assessed in control, MPs, AuNP, SF, MP-SF, RT, RT-AuNP, and RT-MPSF@AuNP-treated Hepa 1–6 cells at 24, 48, and 72 hours. The results are the mean ± SEM of three replicates. (**D**) Healing rates were assessed in control, MPs, AuNP, SF, MP-SF, RT, RT-AuNP, and RT-MPSF@AuNP-treated Hep G2 cells at 24, 48, and 72 hours. The results are the mean of three replicates ± SEM. * represents $P < 0.05$, ** represents $P < 0.01$, *** represents $P < 0.001$, and **** represents $P < 0.0001$.

and 60.76 ± 6.16%, respectively) were significantly higher than those in the SF group (23.56 ± 4.85% and 45.21 ± 4.89%, respectively). The apoptosis rates in the RT-AuNP treatment group (42.71 ± 5.53% and 58.78 ± 1.86%, respectively) were significantly higher than those in the RT group (23.97 ± 2.10% and 45.19 ± 2.19%, respectively). The RT-MPSF@AuNP treatment group exhibited the best apoptosis-inducing effect, with apoptosis rates of 59.14 ± 0.57% and 74.86 ± 1.51% in Hepa 1–6 and Hep G2, respectively. These findings indicate that MP-SF notably amplifies the apoptotic effect of SF on tumor cells. Furthermore, the anti-tumor efficacy is even more pronounced when MPSF@AuNP is used in conjunction with radiotherapy.

In vivo Fluorescence Imaging

ICG and MP-ICG@AuNP were injected into hepatocellular carcinoma-loaded mice via the tail vein, respectively. After 12 h, the mice were analyzed by fluorescence imaging. The results, as shown in Figure S6, revealed that the whole-body fluorescence signals of the mice in the free ICG group were relatively weak, whereas the tumor tissues of the mice in the
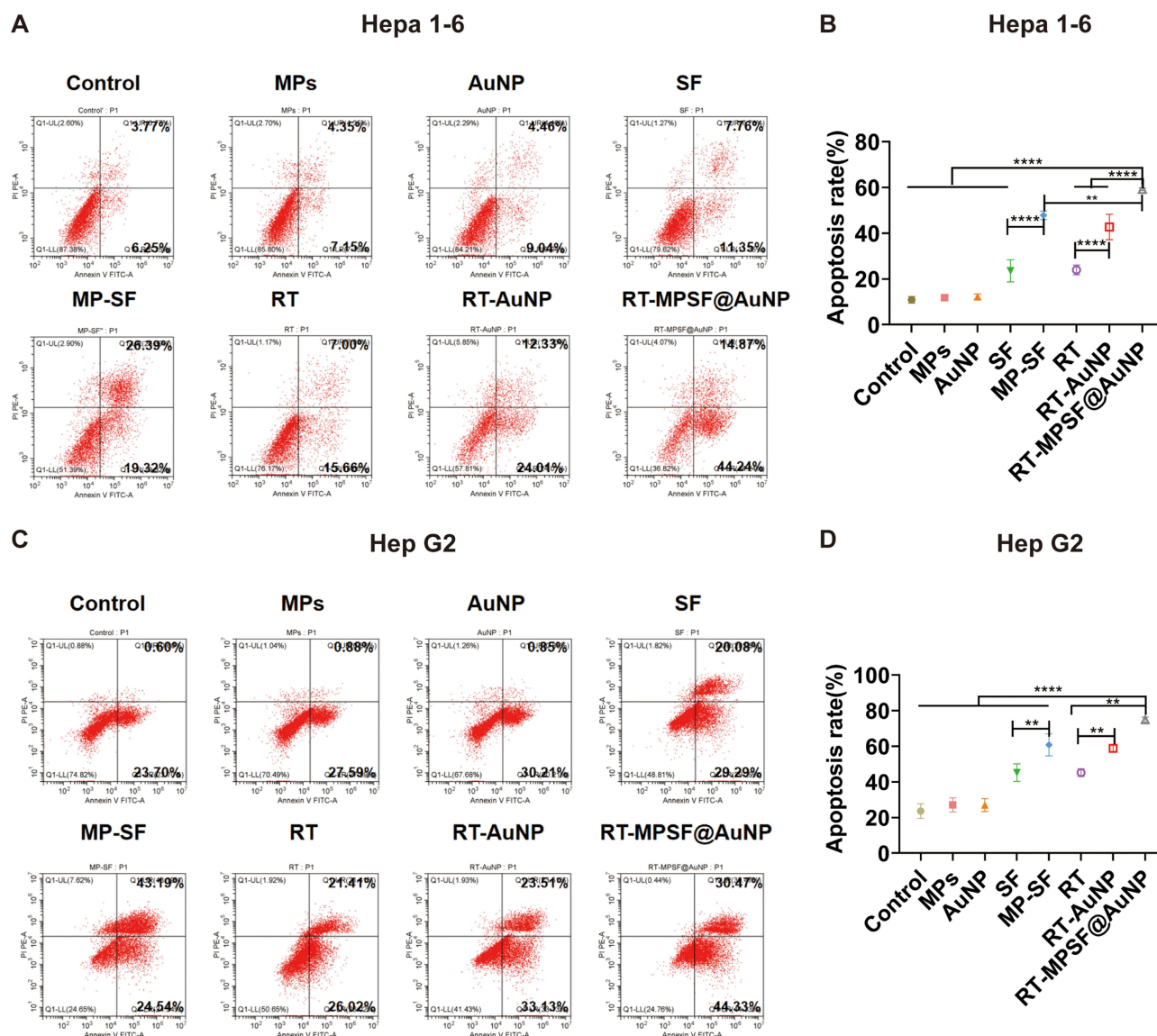
Figure 4 Induction of apoptosis in vitro. (**A**) Flow cytometry analysis was conducted to measure apoptosis in Hepa 1–6 cells treated with control, MPs, AuNP, SF, MP-SF, RT, RT-AuNP, and RT-MPSF@AuNP. (**B**) Quantification of apoptosis in Hepa 1–6 cells by flow cytometry. The results are the mean ± SEM of three replicates. (**C**) Flow cytometry analysis was conducted to measure apoptosis in Hep G2 cells treated with control, MPs, AuNP, SF, MP-SF, RT, RT-AuNP, and RT-MPSF@AuNP. (**D**) Quantification of apoptosis in Hep G2 cells by flow cytometry, the results are the mean ± SEM of three replicates. ** represents $P < 0.01$, and **** represents $P < 0.0001$.

MP-ICG@AuNP group exhibited significantly enhanced fluorescence signals. This result indicated that MP-ICG@AuNP could effectively target tumor tissues and enhance the targeting of free drug to tumors.

In vivo Anti-Tumor Efficacy of MPSF@AuNP Combined With Radiotherapy

To evaluate the therapeutic effect of MPSF@AuNP combined with radiotherapy on liver cancer in vivo, we subcutaneously inoculated Hepa 1–6 cells into the right thigh of C57BL/6J mice and administered treatment as shown in Figure 5A. Tumor volumes of the mice were measured every two days, and their survival times were recorded. Figure 5B, E and F shows that there were no significant differences in tumor volumes among the control, MPs, and AuNP treatment groups, all demonstrating rapid growth, indicating that both MPs and AuNP have no significant anti-tumor effects. RT and SF treatments had some effect on tumor growth in mice, but these effects were weaker than those observed in the MP-SF and RT-AuNP treatment groups. The combination treatment with RT-MPSF@AuNP exhibited the most pronounced inhibition of tumor growth. We compared the survival rates of mice across different treatment groups. Both RT and SF treatments prolonged the survival of the

mice, with MP-SF and RT-AuNP showing better effects, while the RT-MPSF@AuNP combined radiotherapy group had the longest median survival time of 60 days (Figure 5C). No significant weight loss was observed in the treatment groups, suggesting that the RT-MPSF@AuNP combined treatment has no obvious toxic effects (Figure 5D).

To investigate the early therapeutic effects of MPSF@AuNP combined with radiotherapy, we evaluated the glucose metabolism of tumors in each treatment group (Figure 5G–I). The T/M ratios of SUVmax (T/M = tumor SUVmax/ muscle SUVmax) for the Control, MPs, AuNP, SF, MP-SF, RT, RT-AuNP, and RT-MPSF@AuNP groups were 3.00 ± 0.10, 2.93 ± 0.21, 3.03 ± 0.06, 2.33 ± 0.06, 1.43 ± 0.21, 2.30 ± 0.17, 1.37 ± 0.06 and 0.82 ± 0.10, respectively. The T/M values of SUVmean followed a similar trend to SUVmax, with values of 2.23 ± 0.12, 2.20 ± 0.30, 2.03 ± 0.25, 1.77 ± 0.23, 1.20 ± 0.10, 1.73 ± 0.06, 0.91 ± 0.10 and 0.66 ± 0.10. The RT-MPSF@AuNP group had the lowest ^{18}FDG uptake, indicating that this group had the best early treatment response. In summary, we found that MP-SF and RT-AuNP can enhance the in vivo anti-tumor effects of SF and RT, respectively, with the combination of RT and MPSF@AuNP showing the best therapeutic effect. This may be due to the SF encapsulated by MPs, which effectively improved tumor targeting and drug absorption, while AuNP enhanced the absorption of radiative energy by tumor cells, resulting in a synergistic killing effect on the tumor cells.

Antitumor Immunomodulatory Effects of Combined Therapy

Histopathological examination revealed that the tumor tissues in the control, MPs, and AuNP groups had relatively intact cellular structures with fewer dead cells (Figure 6A). In contrast, other treatment groups showed significant evidence of
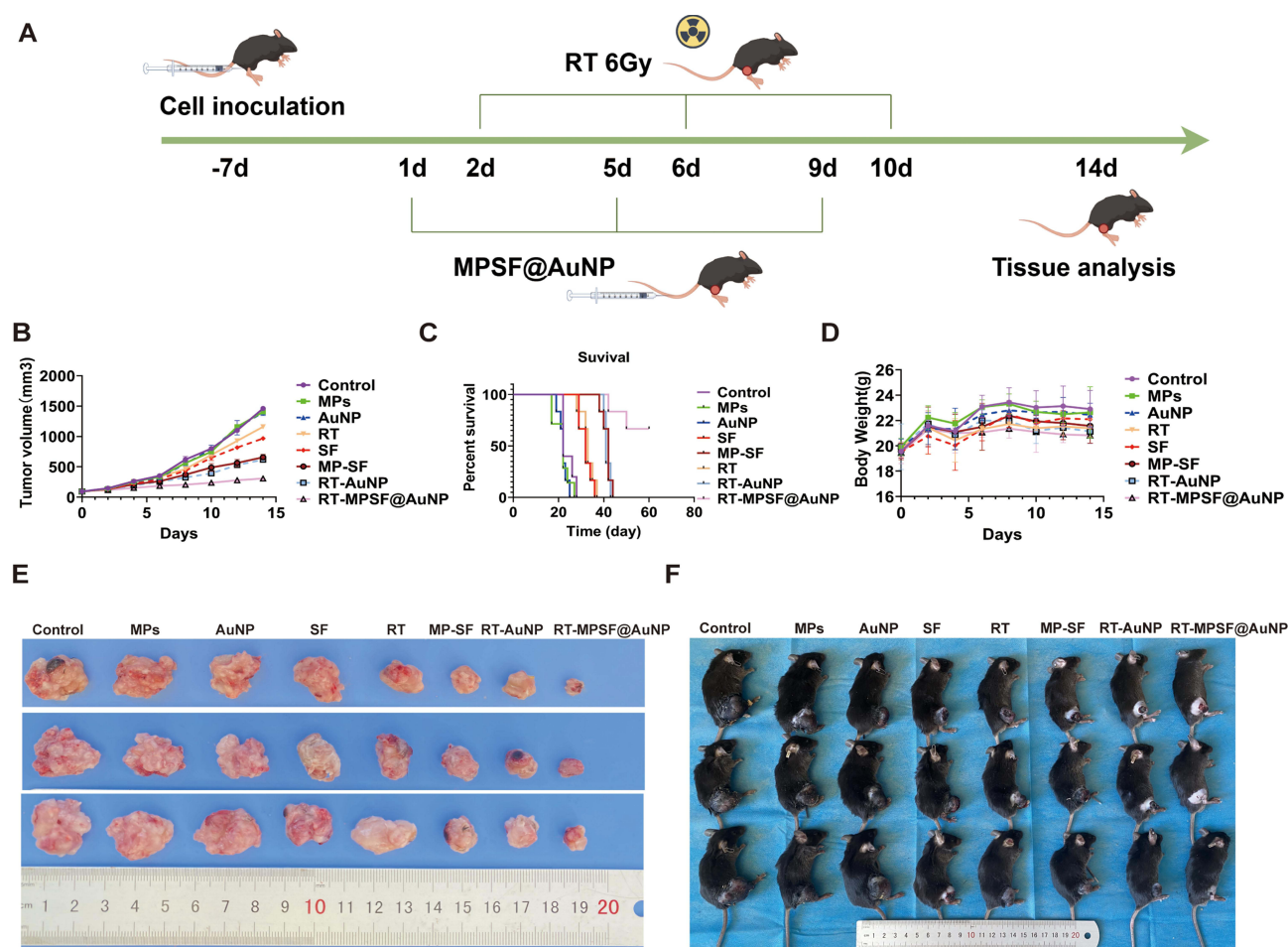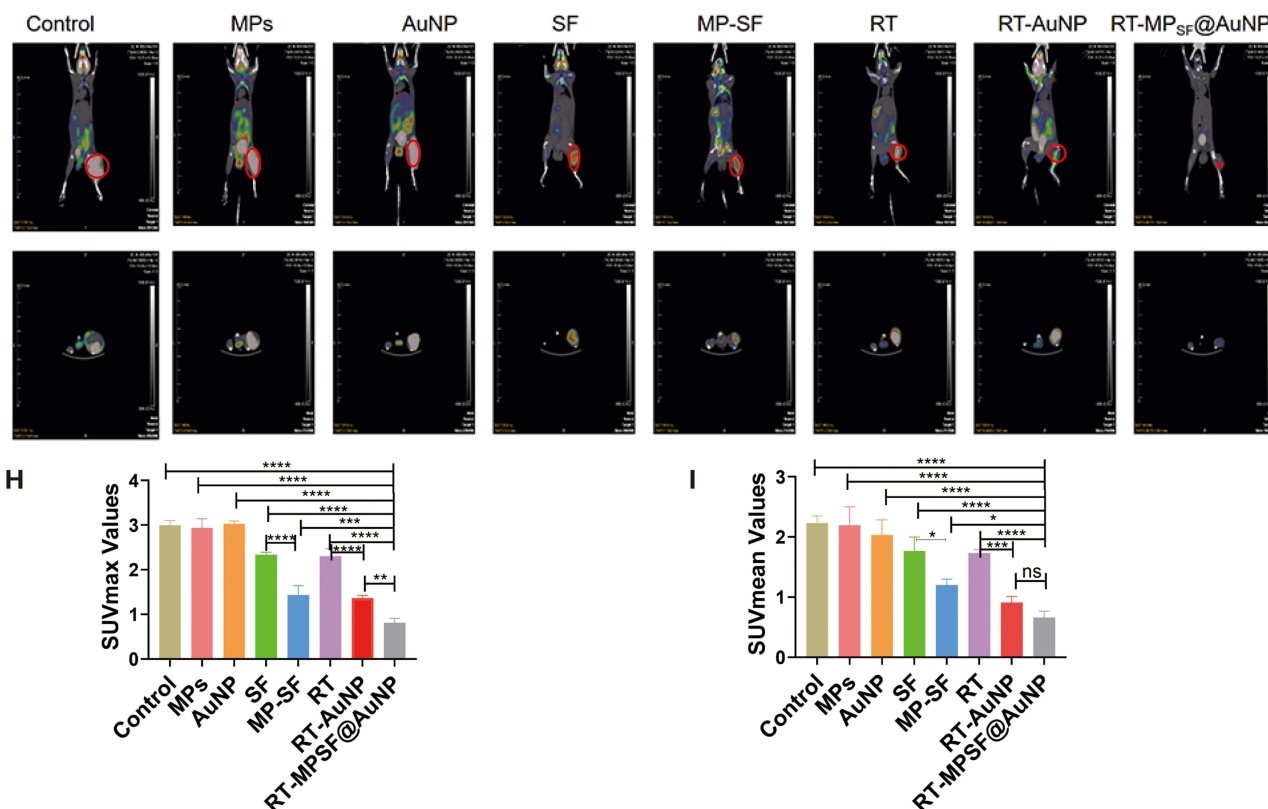

Figure 5 Continued.

G

H

I

Figure 5 In vivo anti-tumor efficacy of MPSF@AuNP combined with radiotherapy. (**A**) In vivo treatment flowchart. (**B**) Changes in tumor volume in mice of different treatment groups (n = 10). (**C**) Survival curves of mice in different treatment groups (n = 10). (**D**) Changes in body weight of mice in different treatment groups (n = 10). (**E**) Representative photographs of Hepa 1–6 tumor-bearing mice in each treatment group on day 14 of treatment. (**F**) Representative photographs of tumors isolated from each treatment group. (**G**) Micro PET/CT scan images of mice on day 14 of treatment. (**H**) Statistical analysis of SUVmax values for each treatment group, the results are the mean ± SEM (n = 3). (**I**) Statistical analysis of SUVmean values for each treatment group, the results are the mean ± SEM (n = 3). * represents $P < 0.05$, ** represents $P < 0.01$, *** represents $P < 0.001$, and **** represents $P < 0.0001$. This image (Figure 5A) was created using Figdraw (https://www.figdraw.com/).

necrotic cells, with the RT-MPSF@AuNP group showing the most pronounced necrosis. Previous studies have indicated that tumor cell-derived MPs contain various antigens from the original cell membrane and endogenous danger signals, while radiotherapy can promote the release of antigens from tumor cells. Therefore, combination therapy has the potential to activate anti-tumor immunity. We assessed the dynamic changes of immune cells in tumors following treatment using immunohistochemical staining. Specifically, we found that the proportion of CD86^{+} cells in the RT-MPSF@AuNP treatment group (9.75±0.50%) was significantly higher than in the other groups (Figure 6A–D). Importantly, compared to the other groups, the proportion of immunosuppressive M2 macrophages (CD206^{+}) in tumor tissues after RT-MPSF@AuNP treatment was significantly reduced (3.92±0.38%) (Figure 6A–E). SF, MP-SF, RT, and RT-AuNP treatments also significantly decreased the proportion of M2 macrophages (CD206^{+}) in the tumors (Figure 6A–E). Additionally, through flow cytometric sorting and immunohistochemistry to detect T lymphocytes in tumor tissues (Figure 6A–C, Figure S7), we observed that the proportion of CD4^{+} and CD8^{+} T cells was higher in the combination therapy group than in the control group and the monotherapy group. These data suggest that, compared to single treatments, MPSF@AuNP combined with radiotherapy can more effectively activate immune cells, reduces the immunosuppressive tumor microenvironment, and induces anti-tumor immune responses.

Evaluation of Toxicity and Side Effects

In vivo safety assessments were conducted to evaluate liver and kidney function, as well as hematological and histopathological changes in each group of mice. Blood samples were collected from mice treated with AuNP, MP-SF, and
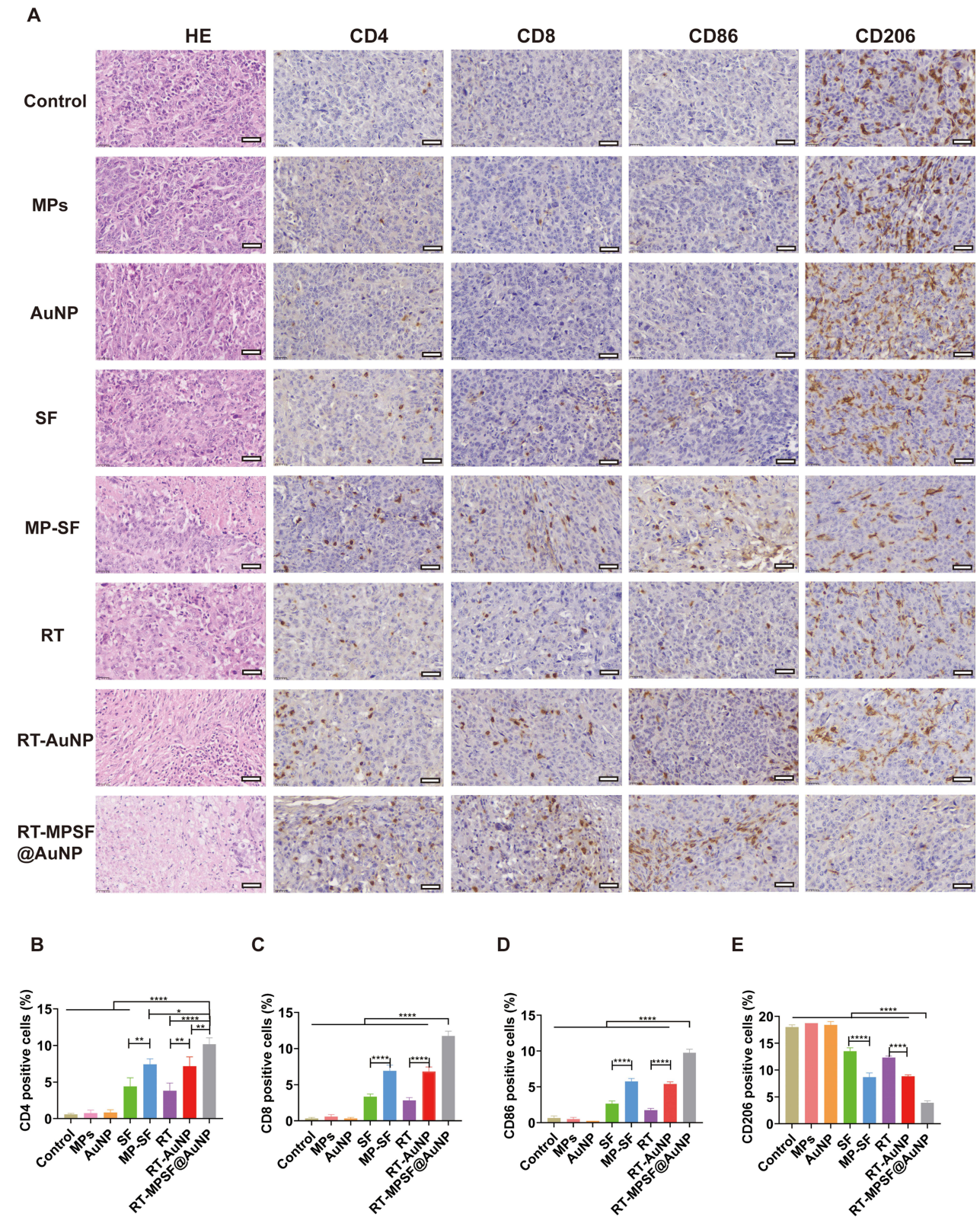
A

Figure 6 The effects of the treatment on immune cell infiltration. (**A**) HE and immunohistochemical staining of tumor tissues. Scale bar, 25 μm. (**B**) Percentage of CD4+ cells in each group (n=3). (**C**) Percentage of CD8+ cells in each group (n=3). (**D**) Percentage of CD86+ cells in each group (n=3). (**E**) Percentage of CD206+ cells in each group (n=3). Data are shown as mean ± SEM. * indicates $P < 0.05$, ** indicates $P < 0.01$, and **** indicates $P < 0.0001$.

MPSF@AuNP. The impact of these treatments on liver and kidney functions, as well as the hematological system, was verified by measuring blood biochemical and routine blood parameters. The biochemical analysis indicated that liver function markers, ALT and AST, in the AuNP, MP-SF, and MPSF@AuNP groups were not significantly different from those in the control group. Similarly, renal function indicators, including ALB, urea, and creatinine, showed no significant differences compared to the control group, suggesting that all formulations did not harm liver or kidney function and exhibited good biosafety (Figure 7A). Routine blood tests revealed that the levels of WBC, RBC, and PLT in the mice treated with AuNP, MP-SF, and MPSF@AuNP were comparable to those of the control group, indicating that these treatments were biologically safe and had no adverse effects on the hematological system (Figure 7B). Furthermore, histological examination through H&E staining of major organs (heart, liver, spleen, lung, and kidney) across all treatment groups displayed no significant signs of cell necrosis (Figure 7C). These results indicate that MPSF@AuNP has good biosafety.

Discussion

Hepatocellular carcinoma (HCC) represents one of the most prevalent malignancies, with a high incidence and mortality rate, ranking third third in global cancer deaths.[59] Current therapeutic modalities for liver cancer include chemotherapy and radio-therapy. Compared to monotherapy approaches, the combination of chemotherapy and radiotherapy shows synergistic anti-tumor benefits.[60] Sorafenib is a molecular targeted therapy drug with dual anticancer properties and is the FDA-approved gold standard for advanced HCC.[3,19,61] Although sorafenib has therapeutic effects on HCC as a monotherapy, its widespread application is limited due to adverse reactions such as diarrhea, rash, alopecia, hand-foot syndrome. Numerous studies have shown that sorafenib has enhanced effects when used in combination with other treatments.[19,62–64] Although radiotherapy constitutes a cornerstone intervention, HCC is moderately sensitive to radiotherapy; thus, the therapeutic effect of radiotherapy alone on HCC is relatively limited.[65,66] In this investigation, we engineered a microparticle-based co-delivery system (MPSF@AuNP) encapsulating sorafenib with gold nanoparticles to address dual challenges: enhancing drug solubility and tumor targeting while leveraging AuNP-mediated radiation dose amplification for radio sensitization. Crucially, tumor cell-derived microparti-cles (MPs) retain homologous membrane architecture and exhibit inherent biocompatibility, rendering them ideal nano vehicles for tumor-selective drug delivery.[67] These vesicles possess advantages such as high safety, stability, and targeting ability, making them promising for clinical cancer treatment.[27,54,55] Consistent with previous studies, we found that MP-SF can target tumor cells and enhance the cytotoxic effects of drugs on these cells. The ability of MP-SF to target and kill tumor cells can be explained by several mechanisms. First, MP-SF exhibits good compatibility with tumor tissue and can circulate in the body for an extended period without being cleared, resulting in a reduced likelihood of uptake and metabolism by other organs.[54] Second, the MPs carrier is rich in lipids and possesses the ability to deform physically, allowing it to easily penetrate the tumor vasculature and reach the target tissue, thereby increasing the uptake rate of SF by tumor cells.[68–70] Additionally, MP-SF can not only deliver drugs into the cells but also inhibit drug efflux by disrupting the ATP-binding cassette transporter system, thereby increasing tumor cell death.[27,71,72] Furthermore, MP-SF can exert a "domino-like" cytotoxic effect, meaning that once SF enters the cells, it can trigger tumor cells to produce new MP-SF, thus maintaining continuous cytotoxic activity against the tumor cells.[55,73] In our experimental design, we explored the combinatorial efficacy of MPSF@AuNP co-encapsulating sorafenib and AuNP with radiotherapy for HCC treatment. The dual-modality system synergistically enhances therapeutic outcomes: MPSF optimizes SF cytotoxicity, while AuNP amplify radiotherapy efficacy through localized energy deposition. A significant advantage of this combination therapy is its ability to effectively reverse the immunosuppressive tumor microenvironment and activate anti-tumor immune responses.[74–78] The MPSF@AuNP, which carries targeted therapeutic drugs and gold nanoparticles, can efficiently target and kill tumor cells, thereby improving the tumor microenvironment and downregulating the secretion of immune-suppressive factors by tumor cells. Complementarily, radiotherapy can induce immunogenic cell death (ICD) in tumor cells, leading to the release of tumor-associated antigens (TAAs), damage-associated molecular patterns (DAMPs), cytokines, and chemokines. This cascade of events facilitates tumor antigen presentation and the activation of tumor-specific T cells.[34,35,51,79] This immunostimulatory cascade facilitates tumor antigen presentation and primes tumor-specific T cell responses, establishing a rationale for synergistically augmented antitumor immunity through combinatorial RT-MPSF@AuNP regimens. Our findings indicate that the combination of MPSF@AuNP and radiotherapy significantly increases the infiltration of effective immune cells within tumors, including CD86$^+$ dendritic cells, CD4$^+$ helper T cells, and CD8$^+$ cytotoxic T lymphocytes (CTLs). Notably, we observed a significant reduction in the number of immunosuppressive M2 macrophages (CD206$^+$) in the combined treatment
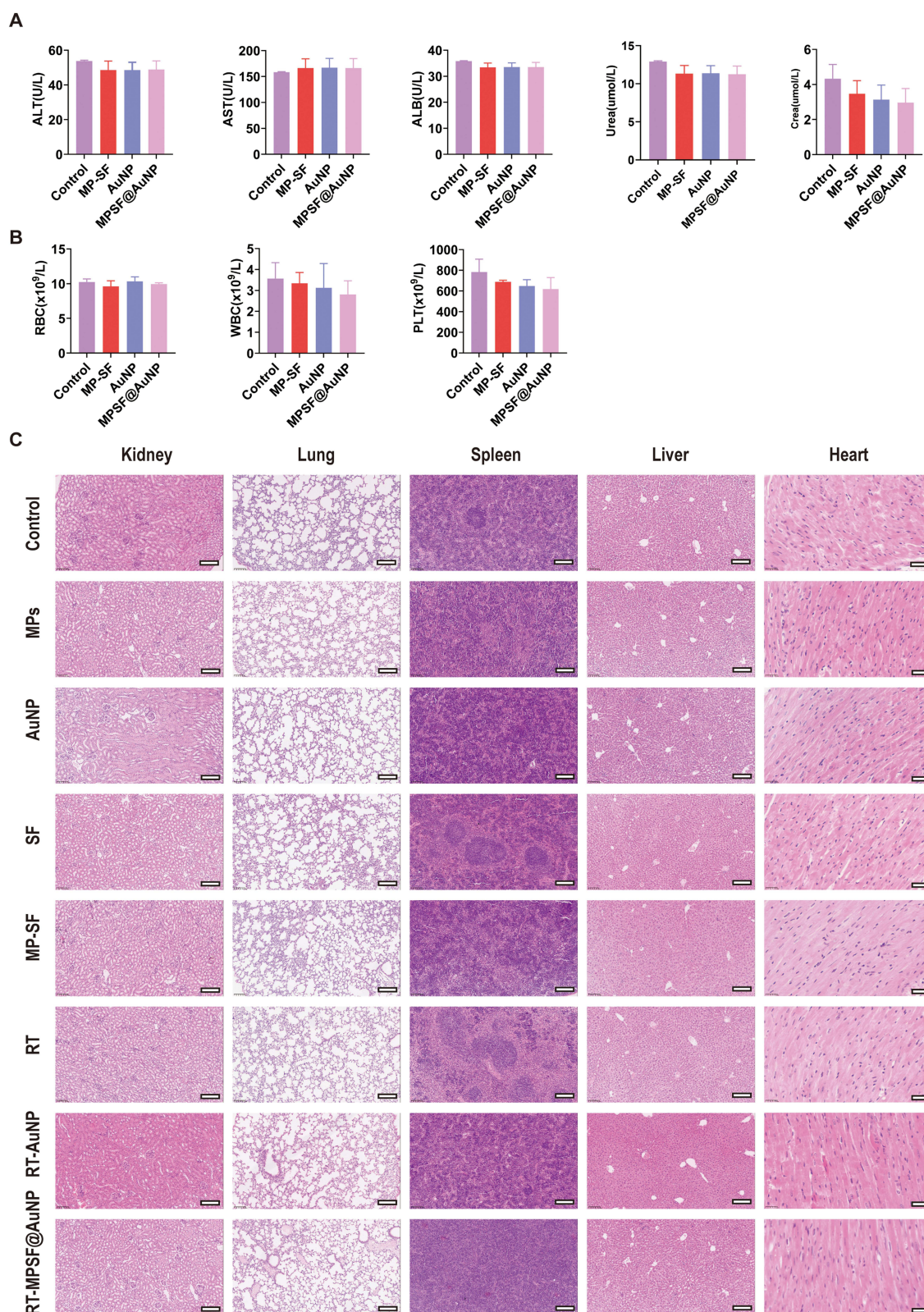
Figure 7 Evaluation of toxicity and side effects. (**A**) Effect of AuNP, MP-SF and MPSF@AuNP on liver function and kidney function (n = 3). (**B**) Effect of AuNP, MP-SF and MPSF@AuNP on haematological indices such as white blood cells (WBC), red blood cells (RBC) and platelets (PLT) (n = 3). (**C**) HE staining analysis of major organs in each treatment group (n=3). Scale bar, 25 μm.

group. This suggests that the therapeutic strategy effectively reverses the immunosuppressive tumor microenvironment and enhances CTL-mediated tumor cell killing, ultimately inhibiting tumor growth. In this study, the combination of MPSF@AuNP with radiotherapy shows a synergistic anti-tumor effect by enhancing the inhibition of tumor cell proliferation, promoting tumor cell apoptosis, remodeling the tumor microenvironment, and activating anti-tumor immune responses.

Conclusion

In this study, MPSF@AuNP derived from hepatocellular carcinoma cells was successfully prepared, which exhibit good safety, high biocompatibility, and strong targeting properties. In vitro and in vivo experimental results confirmed that the combination of MPSF@AuNP and radiotherapy exerts a synergistic anti-liver cancer effect, effectively inhibiting tumor growth. Notably, RT-MPSF@AuNP not only enhances cytotoxic effects against tumor cells but also remodels the tumor microenvironment, activating anti-tumor immune responses. These findings establish a novel combinatorial paradigm for treatment-refractory malignancies like HCC, demonstrating significant translational potential.

Data Sharing Statement

Data will be made available on request.

Author Contributions

All authors made a significant contribution to the work reported, whether that is in the conception, study design, execution, acquisition of data, analysis and interpretation, or in all these areas; took part in drafting, revising or critically reviewing the article; gave final approval of the version to be published; have agreed on the journal to which the article has been submitted; and agree to be accountable for all aspects of the work.

Funding

Disclosure

The authors declared that they have no conflicts of interest to this work. We declare that we do not have any commercial or associative interest that represents a conflict of interest in connection with the work submitted.

References

1. Bray F, Laversanne M, Sung H, et al. Global cancer statistics 2022: GLOBOCAN estimates of incidence and mortality worldwide for 36 cancers in 185 countries. *Ca Cancer J Clinicians*. 2024;74(3):229–263. doi:10.3322/caac.21834
2. Vogel A, Martinelli E, Vogel A. Updated treatment recommendations for hepatocellular carcinoma (HCC) from the ESMO Clinical Practice Guidelines. *Ann Oncol*. 2021;32(6):801–805. doi:10.1016/j.annonc.2021.02.014
3. Vogel A, Cervantes A, Chau I, et al. Hepatocellular carcinoma: ESMO clinical practice guidelines for diagnosis, treatment and follow-up. *Ann Oncol*. 2018;29(Suppl 4):iv238–iv255. doi:10.1093/annonc/mdy308
4. Chen LT, Martinelli E, Cheng AL, et al. Pan-Asian adapted ESMO clinical practice guidelines for the management of patients with intermediate and advanced/relapsed hepatocellular carcinoma: a TOS-ESMO initiative endorsed by CSCO, ISMPO, JSMO, KSMO, MOS and SSO. *Ann Oncol*. 2020;31(3):334–351. doi:10.1016/j.annonc.2019.12.001
5. Nie Y, Li D, Peng Y, et al. Metal organic framework coated MnO(2) nanosheets delivering doxorubicin and self-activated DNAzyme for chemo-gene combinatorial treatment of cancer. *Int J Pharm*. 2020;585:119513. doi:10.1016/j.ijpharm.2020.119513
6. Yi-Wen Z, Mei-Hua B, Xiao-Ya L, Yu C, Jing Y, Hong-Hao Z. Effects of oridonin on hepatic cytochrome P450 expression and activities in PXR-humanized mice. *Biol Pharm Bull*. 2018;41(5):707–712. doi:10.1248/bpb.b17-00882
7. Shen Y, Cheng L, Xu M, et al. SGLT2 inhibitor empagliflozin downregulates miRNA-34a-5p and targets GREM2 to inactivate hepatic stellate cells and ameliorate non-alcoholic fatty liver disease-associated fibrosis. *Metabolism*. 2023;146:155657. doi:10.1016/j.metabol.2023.155657
8. He J, Feng X, Liu Y, et al. Graveoline attenuates D-GalN/LPS-induced acute liver injury via inhibition of JAK1/STAT3 signaling pathway. *Biomed Pharmacother*. 2024;177:117163. doi:10.1016/j.biopha.2024.117163
9. Park JW, Chen M, Colombo M, et al. Global patterns of hepatocellular carcinoma management from diagnosis to death: the BRIDGE study. *Liver Int*. 2015;35(9):2155–2166. doi:10.1111/liv.12818
10. Qin S, Bi F, Gu S, et al. Donafenib versus sorafenib in first-line treatment of unresectable or metastatic hepatocellular carcinoma: a randomized, open-label, parallel-controlled phase II-III trial. *J Clin Oncol*. 2021;39(27):3002–3011. doi:10.1200/jco.21.00163
11. Kudo M, Finn RS, Qin S, et al. Lenvatinib versus sorafenib in first-line treatment of patients with unresectable hepatocellular carcinoma: a randomised Phase 3 non-inferiority trial. *Lancet*. 2018;391(10126):1163–1173. doi:10.1016/s0140-6736(18)30207-1

12. Palmer DH. Sorafenib in advanced hepatocellular carcinoma. *N Engl J Med*. 2008;359(23):2498.

13. Cheng AL, Kang YK, Chen Z, et al. Efficacy and safety of sorafenib in patients in the Asia-Pacific region with advanced hepatocellular carcinoma: a Phase III randomised, double-blind, placebo-controlled trial. *Lancet Oncol*. 2009;10(1):25–34. doi:10.1016/s1470-2045(08)70285-7

14. Llovet JM, Ricci S, Mazzaferro V, et al. Sorafenib in advanced hepatocellular carcinoma. *N Engl J Med*. 2008;359(4):378–390. doi:10.1056/NEJMoa0708857

15. Thomas M. Molecular targeted therapy for hepatocellular carcinoma. *J Gastroenterol*. 2009;44(Suppl 19):136–141. doi:10.1007/s00535-008-2252-z

16. Kane RC, Farrell AT, Madabushi R, et al. Sorafenib for the treatment of unresectable hepatocellular carcinoma. *Oncologist*. 2009;14(1):95–100. doi:10.1634/theoncologist.2008-0185

17. Wilhelm S, Carter C, Lynch M, et al. Discovery and development of sorafenib: a multikinase inhibitor for treating cancer. *Nat Rev Drug Discov*. 2006;5(10):835–844. doi:10.1038/nrd2130

18. Hampton T. Cancer drug trials show modest benefit: drugs target liver, gastric, head and neck cancers. *JAMA*. 2007;298(3):273–275. doi:10.1001/jama.298.3.273

19. Zhu Y-J, Zheng B, Wang H-Y, Chen L. New knowledge of the mechanisms of sorafenib resistance in liver cancer. *Acta Pharmacol Sin*. 2017;38(5):614–622. doi:10.1038/aps.2017.5

20. Pan BT, Johnstone RM. Fate of the transferrin receptor during maturation of sheep reticulocytes in vitro: selective externalization of the receptor. *Cell*. 1983;33(3):967–978. doi:10.1016/0092-8674(83)90040-5

21. Mathieu M, Martin-Jaular L, Lavieu G, Théry C. Specificities of secretion and uptake of exosomes and other extracellular vesicles for cell-to-cell communication. *Nat Cell Biol*. 2019;21(1):9–17. doi:10.1038/s41556-018-0250-9

22. Ma Y, Zhang X, Liu C, Zhao Y. Extracellular vesicles in cancers: mechanisms, biomarkers, and therapeutic strategies. *Med Comm*. 2024;5(12):e70009. doi:10.1002/mco2.70009

23. Xu C, Jiang C, Li Z, et al. Exosome nanovesicles: biomarkers and new strategies for treatment of human diseases. *Med Comm*. 2024;5(8):e660. doi:10.1002/mco2.660

24. Théry C, Witwer KW, Aikawa E, et al. Minimal information for studies of extracellular vesicles 2018 (MISEV2018): a position statement of the international society for extracellular vesicles and update of the MISEV2014 guidelines. *J Extracell Vesicles*. 2018;7(1):1535750. doi:10.1080/20013078.2018.1535750

25. Liang Q, Bie N, Yong T, et al. The softness of tumour-cell-derived microparticles regulates their drug-delivery efficiency. *Nat Biomed Eng*. 2019;3(9):729–740. doi:10.1038/s41551-019-0405-4

26. S ELA, Mager I, Breakefield XO, Wood MJ. Extracellular vesicles: biology and emerging therapeutic opportunities. *Nat Rev Drug Discov*. 2013;12(5):347–357. doi:10.1038/nrd3978

27. Ma J, Zhang Y, Tang K, et al. Reversing drug resistance of soft tumor-repopulating cells by tumor cell-derived chemotherapeutic microparticles. *Cell Res*. 2016;26(6):713–727. doi:10.1038/cr.2016.53

28. Lee TH, D'Asti E, Magnus N, Al-Nedawi K, Meehan B, Rak J. Microvesicles as mediators of intercellular communication in cancer–the emerging science of cellular 'debris'. *Semin Immunopathol*. 2011;33(5):455–467. doi:10.1007/s00281-011-0250-3

29. Quesenberry PJ, Aliotta JM. Cellular phenotype switching and microvesicles. *Adv Drug Deliv Rev*. 2010;62(12):1141–1148. doi:10.1016/j.addr.2010.06.001

30. Zhang H, Huang B. Tumor cell-derived microparticles: a new form of cancer vaccine. *Oncoimmunology*. 2015;4(8):e1017704. doi:10.1080/2162402x.2015.1017704

31. Baumann M, Krause M, Overgaard J, et al. Radiation oncology in the era of precision medicine. *Nat Rev Cancer Apr*. 2016;16(4):234–249. doi:10.1038/nrc.2016.18

32. Atun R, Jaffray DA, Barton MB, et al. Expanding global access to radiotherapy. *Lancet Oncol*. 2015;16(10):1153–1186. doi:10.1016/S1470-2045(15)00222-3

33. Sevenich L. Turning "cold" into "hot" tumors-opportunities and challenges for radio-immunotherapy against primary and metastatic brain cancers. *Front Oncol*. 2019;9:163. doi:10.3389/fonc.2019.00163

34. Filatenkov A, Baker J, Mueller AM, et al. Ablative tumor radiation can change the tumor immune cell microenvironment to induce durable complete remissions. *Clin Cancer Res*. 2015;21(16):3727–3739. doi:10.1158/1078-0432.Ccr-14-2824

35. Gupta A, Probst HC, Vuong V, et al. Radiotherapy promotes tumor-specific effector CD8+ T cells via dendritic cell activation. *J Immunol*. 2012;189(2):558–566. doi:10.4049/jimmunol.1200563

36. Lugade AA, Moran JP, Gerber SA, Rose RC, Frelinger JG, Lord EM. Local radiation therapy of B16 melanoma tumors increases the generation of tumor antigen-specific effector cells that traffic to the tumor. *J Immunol*. 2005;174(12):7516–7523. doi:10.4049/jimmunol.174.12.7516

37. Matsumura S, Wang B, Kawashima N, et al. Radiation-induced CXCL16 release by breast cancer cells attracts effector T cells. *J Immunol*. 2008;181(5):3099–3107. doi:10.4049/jimmunol.181.5.3099

38. Álvarez-Camacho M, Gonella S, Campbell S, Scrimger RA, Wismer WV. A systematic review of smell alterations after radiotherapy for head and neck cancer. *Cancer Treat Rev*. 2017;54:110–121. doi:10.1016/j.ctrv.2017.02.003

39. Chen Y, Yang J, Fu S, Wu J. Gold nanoparticles as radiosensitizers in cancer radiotherapy. *Int J Nanomed*. 2020;15:9407–9430. doi:10.2147/ijn.S272902

40. Wang H, Mu X, He H, Zhang X-D. Cancer radiosensitizers. *Trends Pharmacol Sci*. 2018;39(1):24–48. doi:10.1016/j.tips.2017.11.003

41. Zhang XD, Luo Z, Chen J, et al. Ultrasmall Au(10-12)(SG)(10-12) nanomolecules for high tumor specificity and cancer radiotherapy. *Adv Mater*. 2014;26(26):4565–4568. doi:10.1002/adma.201400866

42. Cui L, Her S, Borst GR, Bristow RG, Jaffray DA, Allen C. Radiosensitization by gold nanoparticles: will they ever make it to the clinic? *Radiother Oncol*. 2017;124(3):344–356. doi:10.1016/j.radonc.2017.07.007

43. Yang H, Fung SY, Xu S, et al. Amino acid-dependent attenuation of toll-like receptor signaling by peptide-gold nanoparticle hybrids. *ACS Nano*. 2015;9(7):6774–6784. doi:10.1021/nn505634h

44. Zhang XD, Wu D, Shen X, Liu PX, Fan FY, Fan SJ. In vivo renal clearance, biodistribution, toxicity of gold nanoclusters. *Biomaterials*. 2012;33(18):4628–4638. doi:10.1016/j.biomaterials.2012.03.020

45. Zhang XD, Luo Z, Chen J, et al. Ultrasmall glutathione-protected gold nanoclusters as next generation radiotherapy sensitizers with high tumor uptake and high renal clearance. *Sci Rep*. 2015;5(5):8669. doi:10.1038/srep08669

46. Zhang XD, Chen J, Luo Z, et al. Enhanced tumor accumulation of sub-2 nm gold nanoclusters for cancer radiation therapy. *Adv Healthc Mater*. 2014;3(1):133–141. doi:10.1002/adhm.201300189

47. Dai J, Ashrafizadeh M, Aref AR, Sethi G, Ertas YN. Peptide-functionalized, -assembled and -loaded nanoparticles in cancer therapy. *Drug Discov Today*. 2024;29(7):103981. doi:10.1016/j.drudis.2024.103981

48. Wang Y, Xu Y, Song J, et al. Tumor cell-targeting and tumor microenvironment-responsive nanoplatforms for the multimodal imaging-guided photodynamic/photothermal/chemodynamic treatment of cervical cancer. *Int J Nanomed*. 2024;19:5837–5858. doi:10.2147/ijn.S466042

49. Huang X, He T, Liang X, et al. Advances and applications of nanoparticles in cancer therapy. *Med Comm Oncol*. 2024;3(1). doi:10.1002/mog2.67

50. Zhang D, Wu T, Qin X, et al. Intracellularly generated immunological gold nanoparticles for combinatorial photothermal therapy and immunotherapy against tumor. *Nano Lett*. 2019;19(9):6635–6646. doi:10.1021/acs.nanolett.9b02903

51. Qin X, Yang C, Xu H, et al. Cell-derived biogenetic gold nanoparticles for sensitizing radiotherapy and boosting immune response against cancer. *Small*. 2021;17(50):e2103984. doi:10.1002/smll.202103984

52. Hu X, Yu L, Bian Y, et al. Paclitaxel-loaded tumor cell-derived microparticles improve radiotherapy efficacy in triple-negative breast cancer by enhancing cell killing and stimulating immunity. *Int J Pharm*. 2022;632:122560. doi:10.1016/j.ijpharm.2022.122560

53. Gao Y, Zhang H, Zhou N, et al. Methotrexate-loaded tumour-cell-derived microvesicles can relieve biliary obstruction in patients with extrahepatic cholangiocarcinoma. *Nat Biomed Eng*. 2020;4(7):743–753. doi:10.1038/s41551-020-0583-0

54. Guo M, Wu F, Hu G, et al. Autologous tumor cell-derived microparticle-based targeted chemotherapy in lung cancer patients with malignant pleural effusion. *Sci Trans Med*. 2019;11(474). doi:10.1126/scitranslmed.aat5690

55. Tang K, Zhang Y, Zhang H, et al. Delivery of chemotherapeutic drugs in tumour cell-derived microparticles. *Nat Commun*. 2012;3(1):1282. doi:10.1038/ncomms2282

56. Sukkar F, Shafaa M, El-Nagdy M, Darwish W. Polymeric nanocarriers for effective synergistic action of sorafenib tosylate and gold-sensitized gamma radiation against HepG2 cells. *Int J Nanomed*. 2021;16:8309–8321. doi:10.2147/ijn.S331909

57. Gercel-Taylor C, Atay S, Tullis RH, Kesimer M, Taylor DD. Nanoparticle analysis of circulating cell-derived vesicles in ovarian cancer patients. *Anal Biochem*. 2012;428(1):44–53. doi:10.1016/j.ab.2012.06.004

58. Hu Q, Shang L, Wang M, et al. Co-delivery of paclitaxel and interleukin-12 regulating tumor microenvironment for cancer immunochemotherapy. *Adv Healthcare Mater*. 2020;9(10):e1901858. doi:10.1002/adhm.201901858

59. Sung H, Ferlay J, Siegel RL, et al. Global cancer statistics 2020: GLOBOCAN estimates of incidence and mortality worldwide for 36 cancers in 185 countries. *CA Cancer J Clin*. 2021;71(3):209–249. doi:10.3322/caac.21660

60. Allen C, Her S, Jaffray DA. Radiotherapy for cancer: present and future. *Adv Drug Deliv Rev*. 2017;109:1–2. doi:10.1016/j.addr.2017.01.004

61. Pang R, Poon RT. Angiogenesis and antiangiogenic therapy in hepatocellular carcinoma. *Cancer Lett*. 2006;242(2):151–167. doi:10.1016/j.canlet.2006.01.008

62. Ford R, Schwartz L, Dancey J, et al. Lessons learned from independent central review. *Eur J Cancer*. 2009;45(2):268–274. doi:10.1016/j.ejca.2008.10.031

63. Abou-Alfa GK, Johnson P, Knox JJ, et al. Doxorubicin plus sorafenib vs doxorubicin alone in patients with advanced hepatocellular carcinoma: a randomized trial. *JAMA*. 2010;304(19):2154–2160. doi:10.1001/jama.2010.1672

64. Hsu CH, Shen YC, Lin ZZ, et al. Phase II study of combining sorafenib with metronomic tegafur/uracil for advanced hepatocellular carcinoma. *J Hepatol*. 2010;53(1):126–131. doi:10.1016/j.jhep.2010.01.035

65. Yu L, Sun Y, Li J, et al. Silencing the Girdin gene enhances radio-sensitivity of hepatocellular carcinoma via suppression of glycolytic metabolism. *J Exp Clin Cancer Res*. 2017;36(1). doi:10.1186/s13046-017-0580-7

66. Chen Q, Zheng W, Guan J, et al. SOCS2-enhanced ubiquitination of SLC7A11 promotes ferroptosis and radiosensitization in hepatocellular carcinoma. *Cell Death Differ*. 2023;30(1):137–151. doi:10.1038/s41418-022-01051-7

67. Zuo J, Yan H, Qin S, et al. Extracellular vesicles in cancer drug resistance: mechanistic insights and therapeutic implications. *Med Comm Oncol*. 2024;3(4). doi:10.1002/mog2.94

68. Shvedova AA, Kagan VE, Fadeel B. Close encounters of the small kind: adverse effects of man-made materials interfacing with the nano-cosmos of biological systems. *Annu Rev Pharmacol Toxicol*. 2010;50(1):63–88. doi:10.1146/annurev.pharmtox.010909.105819

69. Peng J, Zhao J, Zhao Y, et al. HeLa cell-derived paclitaxel-loaded microparticles efficiently inhibit the growth of cervical carcinoma. *Int J Nanomed*. 2020;15:6409–6420. doi:10.2147/ijn.S246659

70. Hu Y-L, Gao J-Q. Potential neurotoxicity of nanoparticles. *Int J Pharm*. 2010;394(1–2):115–121. doi:10.1016/j.ijpharm.2010.04.026

71. Keon J, Antoniw J, Carzaniga R, et al. Transcriptional adaptation of mycosphaerella graminicola to programmed cell death (PCD) of its susceptible wheat host. *mol Plant Microbe Interact*. 2007;20(2):178–193. doi:10.1094/mpmi-20-2-0178

72. Barnard AS. Nanohazards: knowledge is our first defence. *Nat Mater*. 2006;5(4):245–248. doi:10.1038/nmat1615

73. Mause SF, Weber C. Microparticles: protagonists of a novel communication network for intercellular information exchange. *Circ Res*. 2010;107(9):1047–1057. doi:10.1161/CIRCRESAHA.110.226456

74. Jiang J, Mei J, Yi S, et al. Tumor associated macrophage and microbe: the potential targets of tumor vaccine delivery. *Adv Drug Deliv Rev*. 2022;180:114046. doi:10.1016/j.addr.2021.114046

75. Rao L, Wu L, Liu Z, et al. Hybrid cellular membrane nanovesicles amplify macrophage immune responses against cancer recurrence and metastasis. *Nat Commun*. 2020;11(1):4909. doi:10.1038/s41467-020-18626-y

76. Stathopoulos GT, Kalomenidis I. Malignant pleural effusion: tumor-host interactions unleashed. *Am J Respir Crit Care Med*. 2012;186(6):487–492. doi:10.1164/rccm.201203-0465PP

77. Stathopoulos GT, Psallidas I, Moustaki A, et al. A central role for tumor-derived monocyte chemoattractant protein-1 in malignant pleural effusion. *J Natl Cancer Inst*. 2008;100(20):1464–1476. doi:10.1093/jnci/djn325

78. Sun Y, Zheng Z, Zhang H, et al. Chemotherapeutic tumor microparticles combining low-dose irradiation reprogram tumor-promoting macrophages through a tumor-repopulating cell-curtailing pathway. *Oncoimmunology*. 2017;6(6):e1309487. doi:10.1080/2162402x.2017.1309487

79. Formenti SC, Demaria S. Combining radiotherapy and cancer immunotherapy: a paradigm shift. *J Natl Cancer Inst*. 2013;105(4):256–265. doi:10.1093/jnci/djs629